UCSF

Title

Translation of Carbon-13 EPI for hyperpolarized MR molecular imaging of prostate and brain cancer patients

Authors

Gordon, Jeremy W
Chen, Hsin-Yu
Autry, Adam
et al.

Peer reviewed

Translation of Carbon-13 EPI for Hyperpolarized MR Molecular Imaging of Prostate and Brain Cancer Patients

Jeremy W Gordon[1], **Hsin-Yu Chen**[1], **Adam Autry**[1], **Ilwoo Park**[2], **Mark Van Criekinge**[1], **Daniele Mammoli**[1], **Eugene Milshteyn**[1], **Robert Bok**[1], **Duan Xu**[1], **Yan Li**[1], **Rahul Aggarwal**[3], **Susan Chang**[4], **James B Slater**[1], **Marcus Ferrone**[5], **Sarah Nelson**[1], **John Kurhanewicz**[1], **Peder EZ Larson**[1], and **Daniel B Vigneron**[1]

[1]Department of Radiology and Biomedical Imaging, University of California San Francisco, San Francisco, California

[2]Department of Radiology, Chonnam National University Medical School and Hospital, Gwangju, Korea

[3]Department of Medicine, University of California San Francisco, San Francisco, California

[4]Department of Neurological Surgery, University of California San Francisco, San Francisco, California

[5]Department of Clinical Pharmacy, University of California San Francisco, San Francisco, California

Abstract

Purpose: To develop and translate a metabolite-specific imaging sequence using a symmetric echoplanar readout for clinical hyperpolarized (HP) ^{13}C applications.

Methods: Initial data were acquired from patients with prostate cancer (n=3) and high-grade brain tumors (n=3) on a 3T scanner. Samples of [1-^{13}C]pyruvate were polarized for at least two hours using a 5T SPINlab system operating at 0.8 K. Following injection of the HP substrate, pyruvate, lactate, and bicarbonate (for brain studies) were sequentially excited with a singleband spectral-spatial RF pulse and signal was rapidly encoded with a single-shot echoplanar readout on a slice-by-slice basis. Data were acquired dynamically with a temporal resolution of 2 s for prostate studies and 3 s for brain studies.

Results: High pyruvate signal was seen throughout the prostate and brain, with conversion to lactate being shown across studies, while bicarbonate production was also detected in the brain. No Nyquist ghost artifacts or obvious geometric distortion from the echoplanar readout were observed. The average error in center frequency was 1.2 ± 17.0 and 4.5 ± 1.4 Hz for prostate and brain studies, respectively, below the threshold for spatial shift due to bulk off-resonance.

Conclusion: This study demonstrated the feasibility of symmetric EPI to acquire HP ^{13}C metabolite maps in a clinical setting. As an advance over prior single slice dynamic or single time point volumetric spectroscopic imaging approaches, this metabolite-specific EPI acquisition

Corresponding Author: Jeremy Gordon, 1700 4th St, Byers Hall 102, San Francisco, CA 94158, jeremy.gordon@ucsf.edu, Phone: (415)-514-4454.

provided robust whole-organ coverage for brain and prostate studies while retaining high SNR, spatial resolution, and dynamic temporal resolution.

Introduction

There remains an unmet clinical need for improved molecular imaging techniques that provide relevant detection and characterization of cancer presence and response to therapy (1). An emerging approach for metabolic imaging using magnetic resonance is dissolution dynamic nuclear polarization (DNP, (2)) with ^{13}C enriched substrates. This technique provides as much as 5 orders of magnitude enhancement to nuclear spin polarization, and has been applied to endogenous substrates for non-invasive, real-time hyperpolarized (HP) ^{13}C metabolic imaging in pre-clinical (3–5) cancer models, a phase I clinical trial in prostate cancer patients (6), and proof of concept clinical (7–9) studies. This first-in-man study (6) demonstrated the safety and feasibility of this approach to detect metabolic reprogramming in human cancers that demonstrate increased pyruvate-to-lactate conversion via up-regulated lactate dehydrogenase (LDH) expression. The increased conversion of pyruvate to lactate, an outcome of the aberrant reliance on aerobic glycolysis, is a phenomenon known as the Warburg Effect and is a hallmark of advanced and malignant cancers (10).

The non-recoverable magnetization of these metabolically active HP substrates necessitates imaging sequences that are RF efficient, can rapidly encode both spectral and spatial dimensions, and have a high temporal resolution. The first-in-man phase I trial (6) utilized echo-planar spectroscopic imaging (EPSI) methods for HP ^{13}C data acquisitions. While the acquisition methods used in this study were adequate for establishing safety and feasibility in prostate cancer studies, they were limited to a single slice dynamic acquisition or a single time point volumetric acquisition of the prostate with a limited (8×8 cm^2) field-of-view (FOV). Such inherent limitations hindered its broader application for future human studies.

Clinically relevant dynamic HP ^{13}C imaging with volumetric coverage and imaging of larger organs requires far greater FOV coverage. An alternative approach to acquire HP ^{13}C data was first proposed by Cunningham et al (11) and consisted of a spectral-spatial RF pulse to independently excite each metabolite followed by a rapid, single-shot spiral (12) or echoplanar (11,13) readout. This metabolite-specific approach to HP ^{13}C MRI is an appealing alternative to EPSI since it provides higher temporal resolution, is more robust to motion, and can be scaled to large FOVs without an increase in scan time. Compared to a spiral trajectory, echoplanar readouts are more robust to off-resonance and gradient errors, while issues with Nyquist ghost artifacts can be readily corrected by a reference scan (14) or via an exhaustive search of the phase coefficients (15).

In prior work, a symmetric EPI sequence was developed for HP ^{13}C MRI and tested in preclinical animal models with features based on a clinical ^{1}H EPI product sequence that enabled reconstruction on the scanner (13). Translating this sequence to a clinical setting faces the substantial challenges of encoding a larger volume, along with poorer B_0 homogeneity and increased susceptibility. This can hamper the effectiveness of spectral-spatial RF pulses and potentially lead to geometric distortion. The goal of this project was to further develop and translate this HP ^{13}C EPI sequence to obtain initial data in patients with

prostate and brain tumors in order to investigate the potential value of using this rapid acquisition technology for hyperpolarized ^{13}C MR molecular imaging for clinical evaluation.

Methods

Following IRB and FDA IND approved protocols with informed consent, patient research exams were performed on a 3T MR scanner (MR750, GE Healthcare) with clinical performance gradients (50 mT/m maximum gradient strength, 200 mT/m/ms maximum slew-rate). For the prostate studies, a ^{13}C clamshell coil was used for RF excitation (16) while a ^{1}H/^{13}C endorectal receive coil was used for reception. For the brain studies, a birdcage coil was used for RF excitation and an integrated 32 channel coil was used for reception (17). An 8 M ^{13}C urea phantom embedded in both the endorectal and brain coil was used to set the RF transmit power and center frequency. All datasets were acquired with a ramp-sampled, symmetric echoplanar imaging sequence developed for clinical ^{13}C imaging (13) (Fig. 1). Accompanying spectral-spatial (SPSP) RF pulses were designed using the SPSP RF toolbox (18), which can be accessed at https://github.com/LarsonLab/hyperpolarized-mri-toolbox/.

Sample Preparation & Polarization:

Samples containing 1.47 g of Good Manufacturing Practice (GMP) grade [1-^{13}C]pyruvate (MilliporeSigma Isotec) and 15 mM electron paramagnetic agent (EPA; AH111501, GE Healthcare) were prepared by a pharmacist the morning of the study. Samples were polarized using a 5T clinical polarizer (SPINlab, GE Healthcare) for at least two hours. Following dissolution, the electron paramagnetic agent was removed by filtration and pH, pyruvate and EPA concentrations, polarization, and temperature were measured prior to injection. In parallel, the integrity of the 0.5 μm sterile filter was tested in agreement with manufacturer specifications prior to injection. After release by the pharmacist, a 0.43 mL/kg dose of ~250 mM pyruvate was injected at a rate of 5 mL/s, followed by a 20 mL saline flush (0.9% sodium chloride, Baxter Healthcare Corporation), with the acquisition starting 5 s after the end of saline injection.

Prostate Imaging:

HP ^{13}C images were acquired with an 8×8 mm^2 in-plane resolution (12.8×12.8 cm^2 FOV, 16×16 matrix size), 0.5 cm^3 spatial resolution, TR/TE = 62.5 ms/15.4 ms, echo-spacing = 0.62 ms. Metabolites were sequentially excited with a custom echoplanar single-band spectral-spatial RF pulse (150 Hz FWHM, 600 Hz stopband peak-to-peak) using a variable flip angle scheme (Supporting Information Fig. S1) designed to provide a robust estimate of k_{PL} in the presence of B1+ inhomogeneity (19). The center frequency was calibrated using an 8 M ^{13}C-urea standard embedded in the receive coil. Sixteen 8 mm slices were acquired per timeframe, alternating between pyruvate and lactate (f = 390 Hz) for each multi-slice volume, with an effective 2 s temporal resolution and a total acquisition time of 42 s. To correct for Nyquist ghosting, a reference scan was acquired on the ^{1}H channel prior to ^{13}C imaging (13). Following ^{13}C imaging, non-localized spectra (TR = 3 s, θ = 20°, 10 time-points) were acquired with a 500 μs hard pulse to measure the error in center frequency

calibration. For anatomic reference, T2-weighted ^{1}H images (TR/TE = 6 s/102 ms, 18×18 cm^2 FOV, 384 × 384 matrix, 3 mm slice thickness, 2 averages) were acquired for co-localization with the HP ^{13}C data. As part of the multi-parametric MR exam, diffusion weighted ^{1}H images were acquired with a reduced FOV using single-shot spin-echo EPI. A b = 0 s/mm^2 image was acquired, followed by b = 600 s/mm^2 in 6 directions, with TR/TE = 4 s/52.4 ms, FOV = 19 × 8 cm^2, matrix size = 128 × 64, NEX = 6, sixteen 3 mm slices. The geometric mean for the 6 directions was taken before calculating the ADC.

Brain Imaging:

Whole brain coverage was achieved for HP ^{13}C studies with eight 2 cm slices. In-plane resolution was 1.5 × 1.5 cm^2 (24.0 × 24.0 cm^2 FOV, 16 × 16 matrix), with a TR of 62.5 ms, 21.7 ms TE, and 1.03 ms echo-spacing. Similar to prostate studies, metabolites were sequentially excited with a flyback SPSP RF pulse (130 Hz FWHM, 868 Hz stopband peak-to-peak) using a 20° pyruvate/30° lactate/30° bicarbonate flip angle that was constant through time. The center frequency was alternated between pyruvate, lactate (f = 390 Hz), and bicarbonate (f = −322 Hz) for each volume, with an effective 3 s temporal resolution. Twenty total timeframes per metabolite were acquired, yielding a total imaging time of 60s. Following ^{13}C imaging, non-localized spectra (TR = 3 s, θ = 60°, 8 time-points) were acquired with a 500 μs hard pulse to measure the relative metabolite frequencies. For anatomic reference, T2 fluid-attenuated inversion recovery (FLAIR) ^{1}H images (TR/TE = 6.25 s/142 ms, 25.6 × 25.6 cm^2 FOV, 256 × 256 matrix, 5 mm slice thickness) were acquired for co-localization with the HP ^{13}C data.

Analysis:

All datasets were reconstructed using the Orchestra toolbox (GE Healthcare). Phase coefficients from the reference scan were first applied to the raw k-space data. For the ramp-sampled prostate studies, data were then interpolated to a Cartesian grid prior to Fourier transform. For the multichannel brain data, noise pre-whitening (20) was applied in k-space prior to a sum-of-squares coil combination. The noise covariance matrix was calculated from the final pyruvate timeframe, where no signal was present. Area under the curve (AUC) maps were generated by summing the complex data through time, and all ^{1}H/^{13}C overlay images were generated using SIVIC (21).

Results

Prostate Studies

The RF transmit power was determined using the 8 M ^{13}C urea phantom embedded in the coil. Imaging the phantom with the pyruvate flip schedule (Supporting Information Fig. S1) confirmed the RF power calibration and phase correction coefficients prior to hyperpolarized imaging. The center frequency was also set based on the ^{13}C urea phantom and directly measured from the spectra acquired after the end of imaging. The average error in center frequency calibration in the prostate studies was 1.2 ± 17.0 Hz (Supporting Information Table S1), well within the passband for excitation (150 Hz FWHM) and substantially smaller than the bandwidth in the blip dimension (101 Hz/pixel). From the dynamic time series, the peak SNR for pyruvate and lactate was 30.7 ± 12.3 and 7.9 ± 1.4, respectively.

Area under the curve maps (Fig. 2) for pyruvate and lactate provide complete coverage from the base to the apex of the prostate with $8 \times 8 \times 8$ mm^3 (0.5 cm^3) spatial resolution. Nyquist ghost artifacts that could arise from mismatch between even and odd lines of k-space were not observed. These were readily corrected for with the use of the reference scan acquired on the ^{1}H channel, eliminating the need to directly acquire a reference scan from the hyperpolarized ^{13}C magnetization. There is good spatial agreement between regions of elevated total lactate and low ^{1}H ADC, consistent with biopsy-proven Gleason 3+4 cancer in this patient.

Brain Studies

The 4D dynamics for pyruvate, lactate, and bicarbonate (Supporting Information Fig. S2-S4) were also free of apparent geometric distortion and Nyquist ghost artifacts, despite the larger FOV and greater potential for substantial B$_0$ inhomogeneity across the brain. This particular patient had a grade 2 oligodendroglioma and received a subtotal resection 5 years ago. Recent progression was observed on the ^{1}H FLAIR data, and this scan was acquired prior to radiotherapy. The pyruvate signal predominantly reflects the vasculature, with the strongest signal intensity occurring in the superior sagittal sinus and transverse sinuses. Pyruvate conversion to lactate was observed throughout the brain and subcutaneous tissues (**Figs. 3 and 4**). Conversion to bicarbonate demonstrated a different spatial distribution, with highest apparent signal in gray matter and lower relative intensities in white matter and subcutaneous tissues. Quantitatively, the peak SNR for pyruvate, lactate, and bicarbonate was 415.0 ± 27.9, 24.7 ± 7.6, and 7.0 ± 1.0, respectively (Table 1). In all three studies, pyruvate signal was present at the start of the acquisition, which began 5 s after the end of the 20 mL saline flush.

Similar to the prostate studies, the center frequency for hyperpolarized brain studies was also set based on the ^{13}C urea phantom embedded in the coil and directly measured from the spectra acquired after the end of imaging. The average error in center frequency calibration for these studies was 4.5 ± 1.4 Hz (Table 1), well within the passband for excitation (130 Hz FWHM) and substantially smaller than the bandwidth in the blip dimension (61 Hz/pixel).

Discussion

The goal of this study was to translate and investigate the feasibility of a new frequency-specific EPI approach designed for human studies to acquire HP ^{13}C metabolite images from cancer patients. In this research, we acquired first-ever volumetric data of HP [1-^{13}C]pyruvate and its metabolic products [1-^{13}C]lactate and ^{13}C-bicarbonate using a multi-slice, single-shot echoplanar readout in initial prostate cancer and brain cancer patients. Dynamic imaging and whole-organ coverage are crucial in translating this technology for clinical studies. This approach represents a significant advantage over prior single slice acquisitions by enabling greater coverage of tumor location(s) and over single time-point approaches that preclude kinetic rate measurements. The latter is important since simple ratio calculations are time dependent and sub-optimal since patient variations in perfusion can introduce quantification errors in ratio calculations. In the phase 1 trial of prostate cancer patients (6), one approach used was a 2D dynamic EPSI sequence to acquire

a single slice (10×10 mm^2 in-plane resolution, 12 – 40 mm through-plane) every 5 s. Another approach used a single time point 3D EPSI to acquire an entire volume with 0.5 cm^3 spatial resolution over 8–12 s with an FOV of approximately 8×8 cm^2. In contrast, the EPI approach investigated in this study enabled both improved temporal resolution (2 s resolution for prostate studies and 3 s resolution for brain studies) and whole-organ coverage ($12.8 \times 12.8 \times 12.8$ cm^3 for the prostate, $24 \times 24 \times 16$ cm^3 for the brain) without sacrificing spatial coverage or temporal resolution.

The dynamic time course and area under the curve (AUC) maps of pyruvate metabolism in the brain highlights the ability of HP ^{13}C-pyruvate EPI to detect multiple biochemical conversions with multi-slice volumetric coverage of the entire brain for the first time. The differential metabolism observed between gray and white matter may be due to physiological differences or the coil reception profile, which accentuates signal from the cortex and subcutaneous tissue closest to the receive array. Nevertheless, the peak SNR was nearly an order of magnitude higher for pyruvate than for lactate or bicarbonate in the three initial brain studies. This difference in signal provides a potential opportunity to improve SNR for bicarbonate and lactate by optimizing the flip angle for each metabolite (22,23). Ultimately, the achievable spatial resolution will be determined by the metabolite of interest with the lowest SNR, which was bicarbonate in the three patient studies performed here.

The multichannel brain data in this work were combined using a sum-of-squares approach. This resulted in spatial intensity variation throughout the raw images due to the receive profile of each coil. While this variation is implicitly removed when computing the apparent rate constant or AUC ratio map, the individual dynamic images reflect the sensitivity profile of the 32-channel array. This non-uniform intensity could potentially be corrected using fiducial markers to analytically calculate the reception profile using the Biot-Savart law (24), from coil sensitivity maps obtained from a thermal ^{13}C phantom, or from reception profiles extracted from the fully-sampled hyperpolarized data using ESPIRiT (25). Improved coil combination methods (26) could also be used to improve image quality over the conventional sum-of-squares approach used in this work.

While the specific absorption rate (SAR) is nucleus independent (27), the lower ^{13}C gyromagnetic ratio places greater demands on gradient performance, potentially resulting in long ramp times at maximum slew-rate which may cause peripheral nerve stimulation (PNS). Using a low bandwidth readout or increasing the rise time will minimize PNS but will further increase the echo-spacing, increasing the sensitivity to off-resonance. The ability to accurately set the transmit center frequency is therefore crucial to the success of this approach, as off-resonance can impact the effectiveness of SPSP RF pulses because of their narrow passband and can result in a bulk shift in the phase-encode (blip) dimension for EPI studies. The frequencies measured based on residual HP ^{13}C signal after the EPI acquisition indicated that this was not a substantial effect in these studies. EPI shift artifacts due to larger receive frequency errors can be corrected for by phase-modulating the data in k-space or by reversing the blip polarity every other timeframe (28). For setups where a urea phantom is impractical, the center frequency can also be calibrated using the water frequency. In this case, a B1+ map could be acquired from the hyperpolarized substrate using a Bloch-Siegert approach (29) to calibrate the transmit power. Conversely, the transmit

B1 field would not be uniform when using a surface coil for excitation. While a urea phantom could still be used for power calibration, it would require a known, pre-measured change in power to provide the desired flip angle at depth.

Finally, in these initial studies the total readout time for each slice was 9.9 ms for prostate studies and 16.5 ms for brain studies. While this resulted in short echo-spacing and made the acquisitions more robust to B0 inhomogeneity, we anticipate that the SNR could readily be improved by increasing the total readout duration, given the relatively long T_2* of ^{13}C substrates (30). However, this will place more of a burden on shimming and frequency calibration, as a further increase in echo-spacing would make the acquisition more susceptible to geometric distortion and bulk shifts in the blip dimension. In this case, alternating the blip polarity each timeframe (31) or employing a dual-echo EPI acquisition (32,33) could potentially be used to correct for distortion and signal loss arising from B0 inhomogeneity.

Conclusion

This study demonstrated the feasibility of symmetric EPI to acquire hyperpolarized ^{13}C metabolite maps in brain and prostate cancer patients. As an advance over prior spectroscopic imaging approaches, this metabolite-specific EPI acquisition provided robust whole organ coverage for brain and prostate studies while retaining high SNR, spatial resolution and dynamic temporal resolution.

Supplementary Material

Refer to Web version on PubMed Central for supplementary material.

Acknowledgements

References

1. Kurhanewicz J, Vigneron DB, Brindle K, Chekmenev EY, Comment A, Cunningham CH, DeBerardinis RJ, Green GG, Leach MO, Rajan SS, Rizi RR, Ross BD, Warren WS, Malloy CR. Analysis of Cancer Metabolism by Imaging Hyperpolarized Nuclei: Prospects for Translation to Clinical Research. Neoplasia 2011;13(2):81–97. [PubMed: 21403835]

2. Ardenkjær-Larsen JH, Fridlund B, Gram A, Hansson G, Hansson L, Lerche MH, Servin R, Thaning M, Golman K. Increase in signal-to-noise ratio of > 10,000 times in liquid-state NMR. Proc Natl Acad Sci USA 2003;100(18):10158–10163. [PubMed: 12930897]

3. Albers MJ, Bok R, Chen AP, Cunningham CH, Zierhut ML, Zhang VY, Kohler SJ, Tropp J, Hurd RE, Yen Y-F, Nelson SJ, Vigneron DB, Kurhanewicz J. Hyperpolarized 13C Lactate, Pyruvate, and Alanine: Noninvasive Biomarkers for Prostate Cancer Detection and Grading. Cancer Res 2008;68(20):8607–8615. [PubMed: 18922937]

4. Golman K, Zandt Rit, Lerche M, Pehrson R, Ardenkjaer-Larsen JH. Metabolic Imaging by Hyperpolarized 13C Magnetic Resonance Imaging for In vivo Tumor Diagnosis. Cancer Research 2006;66(22):10855–10860. [PubMed: 17108122]

5. Day SE, Kettunen MI, Gallagher FA, Hu DE, Lerche M, Wolber J, Golman K, Ardenkjaer-Larsen JH, Brindle KM. Detecting tumor response to treatment using hyperpolarized 13C magnetic resonance imaging and spectroscopy. Nat Med 2007;13(11):1382–1387. [PubMed: 17965722]

6. Nelson SJ, Kurhanewicz J, Vigneron DB, Larson PEZ, Harzstark AL, Ferrone M, van Criekinge M, Chang JW, Bok R, Park I, Reed G, Carvajal L, Small EJ, Munster P, Weinberg VK, Ardenkjaer-Larsen JH, Chen AP, Hurd RE, Odegardstuen L-I, Robb FJ, Tropp J, Murray JA. Metabolic Imaging of Patients with Prostate Cancer Using Hyperpolarized [1–13C]Pyruvate. Science Translational Medicine 2013;5(198):198ra108.

7. Cunningham CH, Lau JY, Chen AP, Geraghty BJ, Perks WJ, Roifman I, Wright GA, Connelly KA. Hyperpolarized 13C Metabolic MRI of the Human Heart: Initial Experience. Circulation Research 2016.

8. Aggarwal R, Vigneron DB, Kurhanewicz J. Hyperpolarized 1-[13C]-Pyruvate Magnetic Resonance Imaging Detects an Early Metabolic Response to Androgen Ablation Therapy in Prostate Cancer. European Urology.

9. Park I, Larson PEZ, Gordon JW, Carvajal L, Chen H-Y, Bok R, Van Criekinge M, Ferrone M, Slater JB, Xu D, Kurhanewicz J, Vigneron DB, Chang S, Nelson SJ. Development of methods and feasibility of using hyperpolarized carbon-13 imaging data for evaluating brain metabolism in patient studies. Magnetic Resonance in Medicine 2018;80(3):864–873. [PubMed: 29322616]

10. Vander Heiden MG, Cantley LC, Thompson CB. Understanding the Warburg Effect: The Metabolic Requirements of Cell Proliferation. Science 2009;324(5930):1029–1033. [PubMed: 19460998]

11. Cunningham CH, Chen AP, Lustig M, Hargreaves BA, Lupo J, Xu D, Kurhanewicz J, Hurd RE, Pauly JM, Nelson SJ, Vigneron DB. Pulse sequence for dynamic volumetric imaging of hyperpolarized metabolic products. Journal of Magnetic Resonance 2008;193(1):139–146. [PubMed: 18424203]

12. Lau AZ, Chen AP, Ghugre NR, Ramanan V, Lam WW, Connelly KA, Wright GA, Cunningham CH. Rapid multislice imaging of hyperpolarized 13C pyruvate and bicarbonate in the heart. Magnetic Resonance in Medicine 2010;64(5):1323–1331. [PubMed: 20574989]

13. Gordon JW, Vigneron DB, Larson PEZ. Development of a symmetric echo planar imaging framework for clinical translation of rapid dynamic hyperpolarized 13C imaging. Magnetic Resonance in Medicine 2017;77(2):826–832. [PubMed: 26898849]

14. Bruder H, Fischer H, Reinfelder HE, Schmitt F. Image reconstruction for echo planar imaging with nonequidistant k-space sampling. Magnetic Resonance in Medicine 1992;23(2):311–323. [PubMed: 1549045]

15. Wang J, Wright AJ, Hesketh RL, Hu D-e, Brindle KM. A referenceless Nyquist ghost correction workflow for echo planar imaging of hyperpolarized [1–13C]pyruvate and [1–13C]lactate. NMR in Biomedicine 2018;31(2):e3866.

16. Tropp J, Lupo JM, Chen A, Calderon P, McCune D, Grafendorfer T, Ozturk-Isik E, Larson PEZ, Hu S, Yen Y-F, Robb F, Bok R, Schulte R, Xu D, Hurd R, Vigneron D, Nelson S. Multi-channel metabolic imaging, with SENSE reconstruction, of hyperpolarized [1–13C] pyruvate in a live rat at 3.0 tesla on a clinical MR scanner. Journal of Magnetic Resonance 2011;208(1):171–177. [PubMed: 21130012]

17. Mareyam A, Carvajal L, Xu D, Gordon JW, Park I, Vigneron DB, Nelson SJ, Stockmann JP, Keil B, Wald LL. 31-Channel brain array for hyperpolarized 13C imaging at 3T In Proceedings of the 25th Annual Meeting of ISMRM, Honolulu, Hawaii, 2017 Abstract 1225.

18. Larson PEZ, Kerr AB, Chen AP, Lustig MS, Zierhut ML, Hu S, Cunningham CH, Pauly JM, Kurhanewicz J, Vigneron DB. Multiband excitation pulses for hyperpolarized 13C dynamic chemical-shift imaging. Journal of Magnetic Resonance 2008;194(1):121–127. [PubMed: 18619875]

19. Chen H-Y, Larson P, Gordon JW, Bok R, Ferrone M, Van Criekinge M, Carvajal L, Aggarwal R, Slater J, Park I, Milshteyn E, Nelson S, Kurhanewicz J, Vigneron DB. Phase II Clinical Hyperpolarized 13C 3D-Dynamic Metabolic Imaging of Prostate Cancer Using a B1-Insensitive Variable Flip Angle Design In Proceedings of the 25th Annual Meeting of ISMRM, Honolulu, Hawaii, 2017 Abstract 0725.

20. Pruessmann KP, Weiger M, Börnert P, Boesiger P. Advances in sensitivity encoding with arbitrary k-space trajectories. Magnetic Resonance in Medicine 2001;46(4):638–651. [PubMed: 11590639]

21. Crane JC, Olson MP, Nelson SJ. SIVIC: Open-Source, Standards-Based Software for DICOM MR Spectroscopy Workflows. International journal of biomedical imaging 2013;2013:169526.

22. Maidens J, Gordon JW, Arcak M, Larson PEZ. Optimizing flip angles for metabolic rate estimation in hyperpolarized carbon-13 MRI. IEEE Transactions on Medical Imaging 2016;PP(99):1–1. [PubMed: 26151933]

23. Walker CM, Chen Y, Lai SY, Bankson JA. A novel perfused Bloch–McConnell simulator for analyzing the accuracy of dynamic hyperpolarized MRS. Medical Physics 2016;43(4):854–864. [PubMed: 26843246]

24. Dominguez-Viqueira W, Geraghty BJ, Lau JYC, Robb FJ, Chen AP, Cunningham CH. Intensity correction for multichannel hyperpolarized 13C imaging of the heart. Magnetic Resonance in Medicine 2016;75(2):859–865. [PubMed: 26619820]

25. Uecker M, Lai P, Murphy MJ, Virtue P, Elad M, Pauly JM, Vasanawala SS, Lustig M. ESPIRiT— an eigenvalue approach to autocalibrating parallel MRI: Where SENSE meets GRAPPA. Magnetic Resonance in Medicine 2014;71(3):990–1001. [PubMed: 23649942]

26. Zhu Z, Zhu X, Ohliger M, Cao P, Tang S, Gordon J, Carvajal L, Shin P, Aggarwal R, Bok R, Kurhanewicz J, Pamela M, Larson P, Vigneron D. Coil Combination Methods for 16-channel Hyperpolarized 13C Spectroscopic Imaging Studies of Liver Metastases Patients In Proceedings of the 27th Annual Meeting of ISMRM, Paris, France, 2018 Abstract 3881.

27. Haacke EM. Magnetic Resonance Imaging: Physical Principles and Sequence Design: J. Wiley & Sons; 1999.

28. Cunningham CH, Dominguez Viqueira W, Hurd RE, Chen AP. Frequency correction method for improved spatial correlation of hyperpolarized 13C metabolites and anatomy. NMR in Biomedicine 2014;27(2):212–218. [PubMed: 24353129]

29. Lau AZ, Chen AP, Cunningham CH. Integrated Bloch-Siegert B1 mapping and multislice imaging of hyperpolarized 13C pyruvate and bicarbonate in the heart. Magnetic Resonance in Medicine 2012;67(1):62–71. [PubMed: 21656549]

30. Joe E, Lee H, Lee J, Yang S, Choi Y-S, Wang E, Song H-T, Kim D-H. An indirect method for in vivo T2 mapping of [1–13C] pyruvate using hyperpolarized 13C CSI. NMR in Biomedicine 2017;30(5):e3690.

31. Miller JJ, Lau AZ, Tyler DJ. Susceptibility-induced distortion correction in hyperpolarized echo planar imaging. Magnetic Resonance in Medicine 2018;79(5):2135–2141. [PubMed: 28722201]

32. Geraghty BJ, Lau JYC, Chen AP, Cunningham CH. Dual-Echo EPI sequence for integrated distortion correction in 3D time-resolved hyperpolarized 13C MRI. Magnetic Resonance in Medicine 2018;79(2):643–653. [PubMed: 28394085]

33. Lau JYC, Geraghty BJ, Chen AP, Cunningham CH. Improved tolerance to off-resonance in spectral-spatial EPI of hyperpolarized [1–13C]pyruvate and metabolites. Magnetic Resonance in Medicine 2018;80(3):925–934. [PubMed: 29380423]
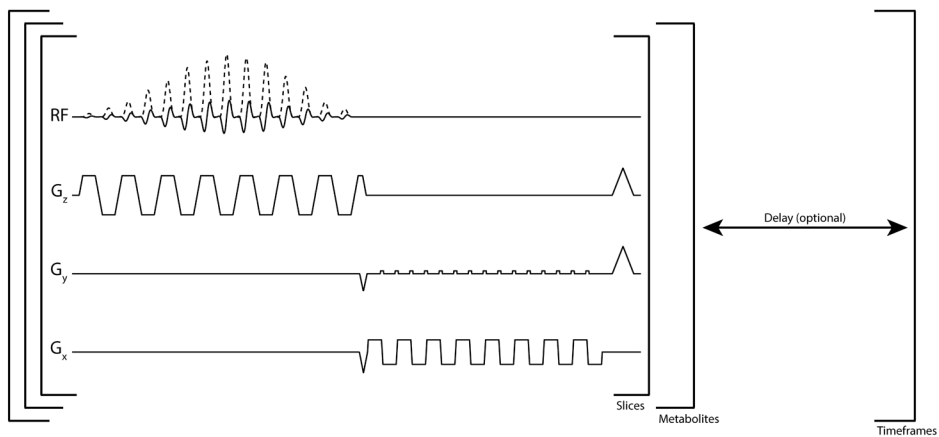
Figure 1.
Multi-slice echoplanar pulse sequence. The complex singleband spectral-spatial pulse (real and imaginary RF shown) is used to selectively excite an individual hyperpolarized metabolite. An entire volume is acquired for one metabolite before switching to the next frequency. An optional delay can be added after all metabolite volumes are acquired to achieve the desired temporal resolution.
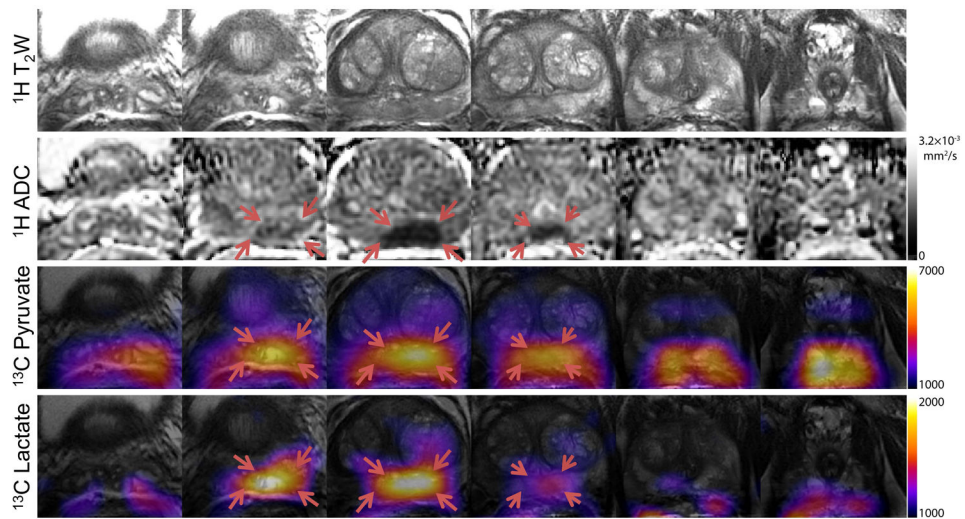
Figure 2.
Anatomic ¹H T₂W and ADC maps, and ¹³C pyruvate and lactate area under the curve
(AUC) maps for the 6 central slices covering the entire prostate, from the base to the apex.
No Nyquist ghost artifacts or geometric distortion were observed in the ¹³C data. There is
good spatial agreement between elevated hyperpolarized lactate and regions of low ¹H ADC
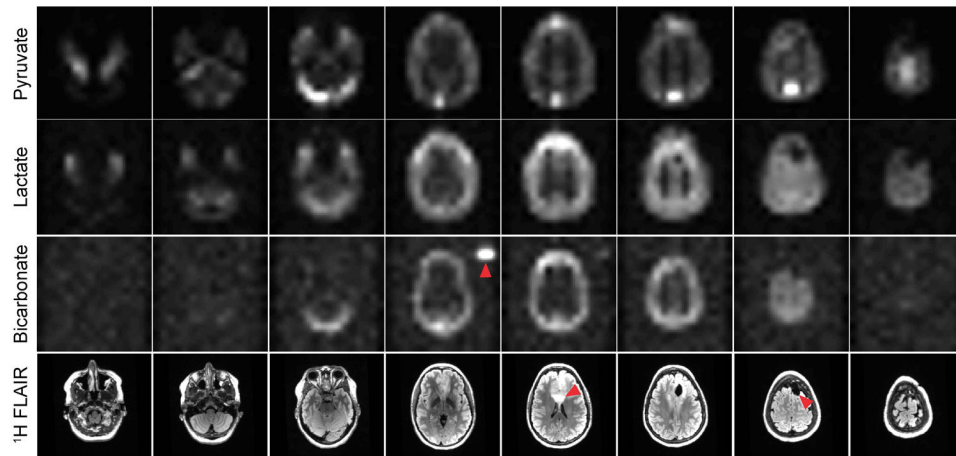(indicated by red arrows), consistent with biopsy-proven Gleason 3+4 cancer.

Figure 3.
Pyruvate, lactate, and bicarbonate area under the curve (AUC) maps for the 8 slices covering the entire brain. The red arrowheads indicate the external ^{13}C urea phantom, ^{1}H FLAIR abnormality, and resection cavity, respectively. [13]C data have been zero-filled fourfold for display. For anatomic reference, [1]H T2 FLAIR images are shown below.
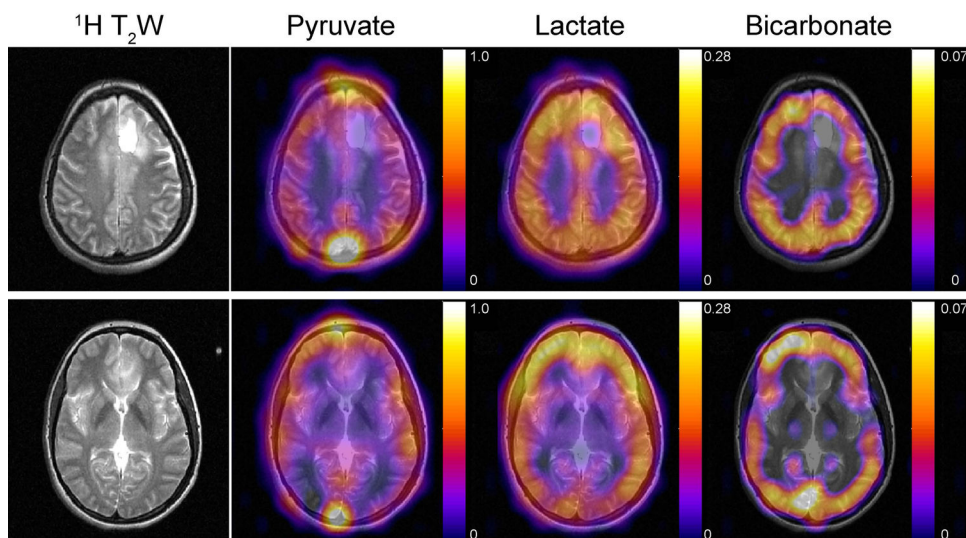
Figure 4.
Pyruvate, lactate, and bicarbonate AUC maps overlaid on ^{1}H T$_2$W images. The AUC maps reflect pyruvate uptake and metabolism over the course of the experiment, with lactate metabolism observed throughout the brain and subcutaneous tissues. Conversion to bicarbonate demonstrated a different spatial distribution, with highest signal in gray matter and relatively lower intensities in white matter and subcutaneous tissues. ^{13}C data were sinc-interpolated to match the resolution of the ^{1}H images, and AUCs were normalized to the peak pyruvate intensity.

Table 1.

Summary of EPI brain studies. All brain data were acquired with 1.5×1.5 cm^2 in-plane resolution using a constant 20° pyruvate/30° lactate/30° bicarbonate flip angle scheme and an integrated birdcage and 32 channel head coil. Time-to-peak (TTP) signal is referenced from the start of acquisition, and the reported polarization is referenced to the start of dissolution. The error in center frequency calibration (f) was measured with non-localized spectroscopy following dynamic imaging.

	f (Hz)	^{13}C Polarization	Time to injection	Pyruvate		Lactate		Bicarbonate	
				Peak SNR	TTP	Peak SNR	TTP	Peak SNR	TTP
Study #1	+3.7	41.3%	54s	447	9s	30	12s	6	15s
Study #2	+3.7	41.9%	60s	396	3s	28	6s	7	9s
Study #3	+6.1	33.1%	53s	402	9s	16	9s	8	15s